1

Homogenisation for elastic photonic crystals and dynamic anisotropy

T. Antonakakis [1,2], R. V. Craster [1], S. Guenneau[3]

[1] *Department of Mathematics, Imperial College London, London SW7 2AZ, UK*
[2] *80 Capital LLP, London, W1S 4JJ, UK*
[3] *Aix-Marseille Université, CNRS, Centrale Marseille, 13013 Marseille, France*

Abstract

We develop a continuum model, valid at high frequencies, for wave propagation through elastic media that contain periodic, or nearly periodic, arrangements of traction free, or clamped, inclusions. The homogenisation methodology we create allows for wavelengths and periodic spacing to potentially be of similar scale and therefore is not limited to purely long-waves and low frequency.

We treat in-plane elasticity, with coupled shear and compressional waves and therefore a full vector problem, demonstrating that a two-scale asymptotic approach using a macroscale and microscale results in effective scalar continuum equations posed entirely upon the macroscale; the vector nature of the problem being incorporated on the microscale. This rather surprising result is comprehensively verified by comparing the resultant asymptotics to full numerical simulations for the Bloch problem of perfectly periodic media. The dispersion diagrams for this Bloch problem are found both numerically and asymptotically. Periodic media exhibit dynamic anisotropy, e.g. strongly directional fields at specific frequencies, and both finite element computations and the asymptotic theory predict this. Periodic media in elasticity can be related to the emergent fields of metamaterials and photonic crystals in electromagnetics and relevant analogies are drawn. As an illustration we consider the highly anisotropic cases and show how their existence can be predicted naturally from the homogenisation theory.

1. Introduction

Wave propagation through elastic periodic, or nearly periodic, media, and their simpler acoustic counterparts (Craster and Guenneau, 2012), are ripe for exploitation using recently developed ideas from photonics and metamaterials in optics. Naturally there have been studies of waves in structured elastic media, with composite fibre media providing motivation. For perfectly periodic media these can be treated using multipole techniques, plane wave expansions or using brute force numerics; the resultant dispersion diagrams (Zalipaev et al., 2002; Guenneau et al., 2003) then show stop-bands and other features highly reminiscent of those from optics. Metamaterials, and structured media such as photonic crystal fibres (Russell, 2003; Zolla et al., 2005), are topical and important subjects in optics, and electromagnetic (EM) waves. The metamaterial field has expanded rapidly since Pendry showed that Veselago's convergent flat lens (Veselago, 1968), overcomes Rayleigh's diffraction limit (Pendry, 2000). This requires simultaneously negative permittivity and permeability, which is an essential condition for a negative refractive index, as demonstrated experimentally by Smith et al. (2000). Photonic crystals have a longer history in optics and EM (John, 1987; Yablonovitch, 1987) and also exhibit useful technological phenomena with their use now widespread (Joannopoulos et al., 2008). The area is almost exclusively preoccupied with electromagnetic (EM) waves, governed by the Maxwell system of equations: it is also clear that similar effects can occur for elasticity (Milton and Nicorovici, 2006; Bigoni et al., 2013), but the elastic case is far less developed than for optics,

[1]corresponding author: r.craster@imperial.ac.uk

and EM, particularly for the vector case of coupled longitudinal-shear in-plane elastic waves. A key ingredient toward developing fundamental understanding of how a microstructured medium behaves is to upscale to an effective medium description.

The classical route to replace a microstructured medium with an effective continuum representation is homogenisation theory, and is detailed in many monographs, Sanchez-Palencia (1980); Bakhvalov and Panasenko (1989); Bensoussan et al. (1978); Panasenko (2005), and essentially relies upon the wavelength being much larger than the microstructure which is usually assumed to be perfectly periodic: this limits the procedure to low frequencies/ long waves and a quasi-static situation, c.f. Parnell and Abrahams (2008); Walpole (1992) for a general setting and Zalipaev et al. (2002) for the specific application to circular holes. Unfortunately for many real applications, particularly in photonics, the limitation to low frequencies is a critical deficiency, nonetheless the attraction of having an effective equation for a microstructured medium where one need no longer model the detail of each individual scatterer and attention can then be given to the overall physics of the structure is highly attractive (Guenneau et al., 2012).

To overcome this limitation a high frequency homogenisation (HFH) technique has been developed, Craster et al. (2010a), to address the scenario when the wavelength and characteristic microstructural lengthscale are of similar order and multiple scattering can be important: a multiple scales approach is utilised, a short microscale and a long macroscale, as in quasi-static homogenisation. This is augmented by utilising some knowledge from physics where it is well-known that a perfectly periodic infinite medium has an exact formulation in terms of Bloch waves, moreover there are standing waves within the periodic setting that occur at discrete standing wave frequencies. The standing wave frequency and eigensolution precisely encode the multiple scattering that occurs and this additional knowledge is then built into the asymptotic procedure. The result is an effective medium theory for periodic, or nearly periodic, media that has no upper frequency limit and thus far it has successfully modelled a variety of multi-scale problems in optics (Craster et al., 2011), discrete lattice media (Craster et al., 2010b), structural mechanics (Nolde et al., 2011), elastic plates (Antonakakis and Craster, 2012) and surface Rayleigh-Bloch (acoustic or EM) waves along multi-scale surfaces (Antonakakis et al., 2013a). The theory emerged from earlier work on high frequency long-wave asymptotics for distorted waveguides (Gridin et al., 2005; Kaplunov et al., 2005), as summarised in Craster et al. (2013), and produces a continuum description posed entirely upon the long-scale, the solution of which modulates a short-scale, possibly highly oscillatory, field; the long-scale equation captures the dynamic anisotropy and features associated with metamaterials and photonic crystal fibres. Thus far the HFH theory is limited to scalar wave systems such as those modelled by the Helmholtz equation, i.e. acoustics, water waves, TE or TM polarised electromagnetic waves and shear horizontal polarised elastic waves, or the extension to a fourth-order elastic plate system. Moving the entire theory to a full vector wave system has several technical and conceptual challenges and the aim of this article is to overcome them.

It is notable that the HFH theory of Craster et al. (2010a) is not alone: there is considerable motivation to create effective continuum models of microstructured media, in various related fields, that break free from the conventional low frequency homogenisation limitations. This desire has created a suite of extended homogenisation theories originating in applied analysis, for periodic media, called Bloch homogenisation (Conca et al., 1995; Allaire and Piatnitski, 2005; Birman and Suslina, 2006; Hoefer and Weinstein, 2011). There is also a flourishing literature on developing homogenised elastic media, with frequency dependent effective parameters, also based upon periodic media (Willis, 2009; Nemat-Nasser et al., 2011; Norris et al., 2012). Those approaches notwithstanding, our aim here is to extend the HFH theory previously only available for scalar Helmholtz or elastic plate cases to the full vector elastic system.

A typical situation might be a finite slab of composite medium, created from equidistant holes or fibres, through which elastic waves then propagate: a schematic is shown in Fig. 1(a) for circular holes, although the methodology is in no way limited to cylindrical defects. If the medium is of large extent, with some lengthscale L, and the holes and their spacing are of lengthscale l, with $l \ll L$, the scale mismatch suggests an asymptotic approach. On the small-scale, attention can be focused on a single elementary cell, shown dashed in Fig. 1(a), and its dynamics are then coupled into the global picture. If a medium is actually infinite and perfectly periodic then the elementary cell truly captures all of the multiple scattering within a framework known as Bloch theory. Here one can assume that there is a phase shift, characterised by a wavenumber vector $\boldsymbol{\kappa}$, and from solid-state physics it is known (Brillouin, 1953; Kittel, 1996) that one

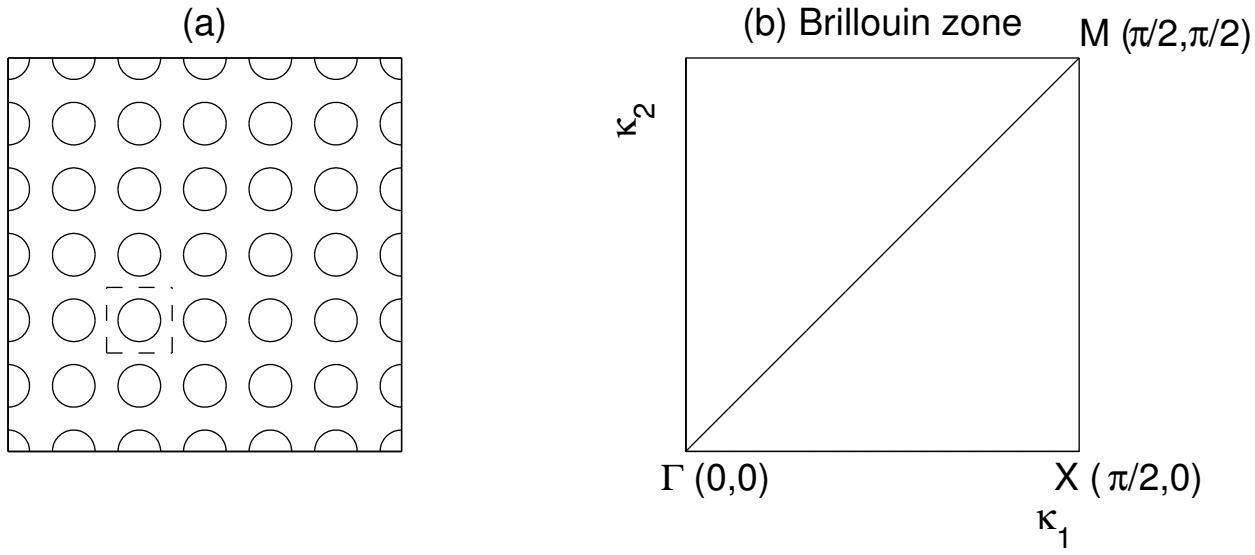

Figure 1: A typical geometry (a) an infinite square array of cylindrical holes with the elementary cell of side 2 shown as the dashed line inner square. In (b) the associated irreducible Brillouin zone is shown, where κ_1 and κ_2 are components of the Bloch vector $\boldsymbol{\kappa}$ which describes the phase shift undergone by an elastic wave moving across the elementary cell.

need only focus attention upon an irreducible Brillouin zone in wavenumber space (shown in Fig. 1(b)) and this representation is useful both within the asymptotic scheme and as a verification of it. In particular, standing waves occur at the edges of the irreducible Brillouin zone (the points Γ, X, M in Fig. 1(b)) and the asymptotic technique uses the behaviour in the neighbourhood of these points to create a long-scale effective medium valid close to the corresponding standing wave frequencies.

In this article we begin, section 2, by formulating the two-scale approach and deriving the effective long-scale partial differential equation (PDE) for a function $f_0(\mathbf{X})$: the PDE contains integrated quantities from the short-scale, but is only posed on the long-scale. For low-frequencies we can generate a long-wave version of the theory and this is briefly described in section 2.4. It is naturally important to verify the asymptotic technique versus full numerical simulations and we proceed to do so in section 3. Initially, asymptotic dispersion curves for the Bloch theory are compared to full numerical simulations, section 3.1, before moving on to look at strongly anisotropic directional waves (section 3.2). We draw together some concluding remarks in section 4.

2. Formulation

We consider an elastic medium punctured by, say, a square array of cylindrical holes although the precise geometry is irrelevant. The inner surface of the holes will be taken here to be either traction free ($\boldsymbol{\sigma}\cdot\mathbf{n}=\mathbf{0}$) or clamped ($\mathbf{u}=\mathbf{0}$) where $\boldsymbol{\sigma}$ is the elastic stress tensor, $\mathbf{u}$ the displacement and $\mathbf{n}$ the outward pointing unit normal from the hole.

The elastic medium is taken to be linear and isotropic with the stress related to the elastic displacements via the constitutive relation

$$\sigma_{ij} = \mu(u_{i,x_j} + u_{j,x_i}) + \lambda\delta_{ij}u_{k,x_k}. \tag{1}$$

The usual Einstein summation convention is adopted and $\mathbf{x} = (x_1, x_2)$ are a Cartesian coordinate system with μ, λ the Lamé parameters and $,x_j$ denoting differentiation with respect to variable x_j. The equation of state, with $\exp(-i\Omega t)$ time dependence assumed and suppressed hereafter, is

$$\sigma_{ij,x_j} + \rho\Omega^2 u_i = 0, \tag{2}$$

and ρ is the density.

To generate the effective description of the medium we follow the methodology given in Craster et al. (2010a) that derives a high-frequency homogenisation theory for general structures in the simpler situation of acoustics or equivalently SH polarised elastic waves. The theory envisages a large array, comprising many microcells each with lengthscale $2l$, with l taken for convenience here to be unity, over a macroscale $L \gg l$; this motivates the introduction of a small positive parameter $\epsilon = l/L \ll 1$ and two spatial variables $\boldsymbol{\xi} = \mathbf{x}$, on the microscale, and $\mathbf{X} = \epsilon\mathbf{x}$, on the macroscale, that are treated independently; this is a multiple scales approach (Bender and Orszag, 1978). This natural separation of scales is augmented by an ansatz for the stresses

$$\sigma_{ij}(\boldsymbol{\xi}, \mathbf{X}) = \sigma_{0ij}(\boldsymbol{\xi}, \mathbf{X}) + \epsilon\sigma_{1ij}(\boldsymbol{\xi}, \mathbf{X}) + \epsilon^2\sigma_{2ij}(\boldsymbol{\xi}, \mathbf{X}) + \dots \tag{3}$$

displacements

$$u_i(\boldsymbol{\xi}, \mathbf{X}) = u_{0_i}(\boldsymbol{\xi}, \mathbf{X}) + \epsilon u_{1i}(\boldsymbol{\xi}, \mathbf{X}) + \epsilon^2 u_{2j}(\boldsymbol{\xi}, \mathbf{X}) + \dots \tag{4}$$

and for the frequency squared

$$\Omega^2 = \Omega_0^2 + \epsilon\Omega_1^2 + \epsilon^2\Omega_2^2 + \dots \tag{5}$$

A key point is that we deliberately make no assumption of the frequency being small: the quasi-static long-wave theory conventionally used in homogenisation theory follows by setting $\Omega^2 = \epsilon^2\Omega_2^2$, see section 2.4, with the consequent simplification that the leading order elastic response, on the microscale, is constant.

Adopting the two-scales approach, and the ansatz above, we obtain a hierarchy of equations, from (2), as

$$\begin{array}{lrcc} O(1): & \sigma_{0_{ij},\xi_j} + \rho\Omega_0^2 u_{0_i} & = & 0 \\ O(\epsilon): & \sigma_{1_{ij},\xi_j} + \rho\Omega_0^2 u_{1_i} & = & -\rho\Omega_1^2 u_{0_i} - \sigma_{0_{ij},X_j} \\ O(\epsilon^2): & \sigma_{2_{ij},\xi_j} + \rho\Omega_0^2 u_{2_i} & = & -\rho\Omega_2^2 u_{0_i} - \rho\Omega_1^2 u_{1_i} - \sigma_{1_{ij},X_j} \end{array} \tag{6}$$

that must be solved order-by-order alongside appropriate boundary conditions. The constitutive relation, (1), rewritten in two-scales as

$$\sigma_{ij} = \mu(u_{i,\xi_j} + u_{j,\xi_i}) + \lambda\delta_{ij}u_{k,\xi_k} + \epsilon(\mu(u_{i,X_j} + u_{j,X_i}) + \lambda\delta_{ij}u_{k,X_k}) \tag{7}$$

also requires expansion. This leads to

$$\begin{array}{lrcc} O(1): & \sigma_{0_{ij}} & = & \mu(u_{0_i,\xi_j} + u_{0_j,\xi_i}) + \lambda\delta_{ij}u_{0_k,\xi_k} \\ O(\epsilon): & \sigma_{1_{ij}} & = & \mu(u_{1_i,\xi_j} + u_{1_j,\xi_i}) + \lambda\delta_{ij}u_{1_k,\xi_k} + \mu(u_{0_i,X_j} + u_{0_j,X_i}) + \lambda\delta_{ij}u_{0_k,X_k} \\ O(\epsilon^2): & \sigma_{2_{ij}} & = & \mu(u_{2_i,\xi_j} + u_{2_j,\xi_i}) + \lambda\delta_{ij}u_{2_k,\xi_k} + \mu(u_{1_i,X_j} + u_{1_j,X_i}) + \lambda\delta_{ij}u_{1_k,X_k}. \end{array} \tag{8}$$

Before settling down to solve this system of equations the boundary conditions must be clearly identified. We consider an elementary cell on the microscale $\boldsymbol{\xi}$, on the hole surface we set either $\mathbf{u} = \mathbf{0}$ or $\boldsymbol{\sigma}\cdot\mathbf{n} = \mathbf{0}$ depending upon whether the holes are clamped inclusions or traction-free holes and we treat both cases simultaneously. More importantly, we need to set boundary conditions on the edges of the cell and at this point we recall that physically there exist standing waves corresponding to waves perfectly in-phase or out-of-phase across the cell. This is shown in the Brillouin zone of Fig. 1(b) and there are three cases to consider: in-phase both horizontally and vertically (Γ), out-of-phase in both directions (M) and in-phase/ out-of-phase in opposite directions (X). These boundary conditions apply on the microscale and so for, say, the in-phase case, we have the stresses periodic in ξ_1 and ξ_2 over each cell, but we do not specify the boundary conditions on the macroscale $\mathbf{X}$.

Returning to the ordered equations (6) the $O(1)$ equation is independent of the long scale and this suggests that the leading order solution is

$$u_{0_i} = f_0(\mathbf{X})U_{0_i}(\boldsymbol{\xi}; \Omega_0). \tag{9}$$

The short-scale displacement field $U_{0_i}(\boldsymbol{\xi}; \Omega_0)$ is entirely on the short-scale and its behaviour is modulated by a long-scale, unknown, function $f_0(\mathbf{X})$. The short-scale displacement field is different for each standing wave frequency Ω_0 and we emphasise this by including it in the argument of the U_{0_i}. It is worth dwelling

on (9) and noting that one could envisage having two different scalar functions f_{0_1}, f_{0_2} multiplying each displacement field or, if one used a potential formulation, the shear and compressional potentials. However, ultimately for self-consistency one is drawn to conclude that $f_{0_1} = f_{0_2}$ and unexpectedly a single scalar function f_0 emerges on the long-scale. The entire aim of this article is to determine the partial differential equation that f_0 obeys and thus to determine the effective long-scale continuum equation describing the punctured elastic medium. Before doing so, we remark that the vector nature of the equations is captured by the vector field $\mathbf{U_0}$ on the short-scale, but the long-scale is described by a scalar function f_0.

Associated with the short-scale displacement, U_{0_i}, is a stress field, $S_{0_{ij}}(\boldsymbol{\xi};\Omega_0)$, defined as

$$S_{0_{ij}} = \mu(U_{0_i,\xi_j} + U_{0_j,\xi_i}) + \lambda\delta_{ij}U_{0_k,\xi_k}. \tag{10}$$

The leading order equation, for the short scale, is then

$$S_{0_{ij},\xi_j} + \rho\Omega_0^2 U_{0_i} = 0 \tag{11}$$

and this can be solved, subject to the boundary conditions, to identify the displacements U_{0i} and stresses S_{0ij}; in the examples treated later these solutions are found numerically.

Moving to first order, the $O(\epsilon)$ equation in (6) has a homogeneous solution which is a multiple of U_0 and this turns out to be irrelevant as it ultimately integrates to zero in later calculations and is henceforth ignored: more importantly there is a particular solution

$$u_{1_i}(\boldsymbol{\xi},\mathbf{X}) = f_{0,X_j}(\mathbf{X})U_{1_{ij}}(\boldsymbol{\xi};\Omega_0). \tag{12}$$

This particular solution involves a tensor function $U_{1_{ij}}$ defined on the short-scale and it is determined as follows. First, we invoke solvability conditions which are a vector version of the Fredholm alternative commonly used in Sturm-Liouville theory. We form a function as the dot product of the $O(\epsilon)$ vector equation (8) with $\mathbf{U}_0$ minus the dot product of the vector equation (11) with $\mathbf{u}_1$ and then the integral of this over an elementary cell S, i.e. in the short-scale, must be zero which leads to

$$\int_S (u_{1_i}S_{0_{ij},\xi_j} - U_{0_i}\sigma_{1_{ij},\xi_j})dS = \int_S (\rho\Omega_1^2 u_{0_i}U_{0_i} + U_{0_i}\sigma_{0_{ij},X_j})dS. \tag{13}$$

Performing these integrals, by using Green's theorem and the boundary conditions, everything eventually cancels except the Ω_1^2 term. This then implies that $\Omega_1^2 = 0$ and it is set to zero, a caveat is that we have implicitly assumed that each standing wave eigenfunction is isolated - repeated roots can, and do, occur and are treated later in sections 2.2, 2.3.

To determine the second order tensor $U_{1_{ij}}$ we require four coupled equations and these emerge from the first order equation in (6): after replacing u_{1_i} with (12), the first order constitutive equation, (8), is split in two such that,

$$\sigma_{1_{ij}} = \sigma^{(1)}_{1_{ij}} + \sigma^{(2)}_{1_{ij}}, \tag{14}$$

where,

$$\sigma^{(1)}_{1_{ij}} = \mu(u_{1_i,\xi_j} + u_{1_j,\xi_i}) + \lambda\delta_{ij}u_{1_k,\xi_k}, \quad \sigma^{(2)}_{1_{ij}} = \mu(u_{0_i,X_j} + u_{0_j,X_i}) + \lambda\delta_{ij}u_{0_k,X_k} \tag{15}$$

so the first term is to be determined whereas the second term contains leading order quantities that are known. The first order equation from (6) is rewritten as,

$$\sigma^{(1)}_{1_{ij},\xi_j} + \rho\Omega_0^2 u_{1_i} = -\sigma_{0_{ij},X_j} - \sigma^{(2)}_{1_{ij},\xi_j}. \tag{16}$$

The four required equations come by writing the stresses back in terms of displacements and we then get four coupled equations for $U_{1_{ij}}$:

$$\mu(U_{1_{11},\xi_j\xi_j} + U_{1_{j1},\xi_1\xi_j}) + \lambda U_{1_{k1},\xi_k\xi_1} + \rho\Omega_0^2 U_{1_{11}} = \quad -(4\mu+2\lambda)U_{0_1,\xi_1} - (\mu+\lambda)U_{0_2,\xi_2} \tag{17}$$

$$\mu(U_{1_{21},\xi_j\xi_j} + U_{1_{j1},\xi_2\xi_j}) + \lambda U_{1_{k1},\xi_k\xi_2} + \rho\Omega_0^2 U_{1_{21}} = \quad -(\mu+\lambda)U_{0_1,\xi_2} - 2\mu U_{0_2,\xi_1} \tag{18}$$

$$\mu(U_{1_{12},\xi_j\xi_j} + U_{1_{j2},\xi_1\xi_j}) + \lambda U_{1_{k2},\xi_k\xi_1} + \rho\Omega_0^2 U_{1_{12}} = \quad -(\mu+\lambda)U_{0_{2},\xi_1} - 2\mu U_{0_{1},\xi_2} \tag{19}$$

$$\mu(U_{1_{22},\xi_j\xi_j} + U_{1_{j2},\xi_2\xi_j}) + \lambda U_{1_{k2},\xi_k\xi_2} + \rho\Omega_0^2 U_{1_{22}} = \quad -(4\mu+2\lambda)U_{0_{2},\xi_2} - (\mu+\lambda)U_{0_{1},\xi_1}\,. \tag{20}$$

Note here we have implicitly assumed that the Lamé parameters are constant over the cell since we treat a single phase periodic problem, but similar equations can be derived for spatially varying μ and λ (heterogeneous λ and μ is a case of practical importance in models of elastic metamaterials, which consist e.g. of soft inclusions in a rigid matrix, or the other way around, in order to achieve some locally resonant behaviours). Equations (17) to (20) are then solved subject to the boundary conditions on an elementary cell.

We now move to second order, the $O(\epsilon^2)$ equation of (6), and adopt a similar approach to that at first order. In particular we form a function that must be zero from solvability and deduce that the following integral over the elementary cell must be satisfied

$$\int_S (u_{2_i} S_{0_{ij},\xi_j} - U_{0_i}\sigma_{2_{ij},\xi_j})dS = \int_S (\rho\Omega_2^2 u_{0_i} U_{0_i} + U_{0_i}\sigma_{1_{ij},X_j})dS. \tag{21}$$

Performing the various integrals over the elementary cell then gives a partial differential equation for the scalar function $f_0(\mathbf{X})$ entirely on the long scale as

$$f_{0,X_kX_j}\int_S \mu(U_{0_i}(U_{1_{ik},\xi_j} + U_{1_{jk},\xi_i}) - U_{1_{ik}}(U_{0_i,\xi_j} + U_{0_j,\xi_i}) + \lambda(U_{1_{ik},\xi_i}U_{0_j} + U_{0_k}U_{0_j} - U_{1_{kj}}U_{0_i,\xi_i}))dS$$
$$+ f_{0,X_jX_j}\int_S \mu U_{0_i}U_{0_i}dS + f_{0,X_iX_j}\int_S \mu U_{0_i}U_{0_j}dS + f_0\Omega_2^2\int_S \rho U_{0_i}U_{0_i}dS = 0. \tag{22}$$

The important point about this equation is that the short-scale is completely absent, it has been integrated out and is encapsulated within coefficients of a rank-2 tensor T_{ij} as (22) can be written as

$$T_{ij}\frac{\partial^2 f_0}{\partial X_i \partial X_j} + \Omega_2^2 f_0 = 0. \tag{23}$$

We will verify this using non-trivial examples later where we use equation (23) to find asymptotic dispersion curves for perfectly periodic Floquet-Bloch problems and compare with full numerical solutions. We stress that we have reduced the complexity of the elasticity problem described by (1) and (2) to solving the scalar PDE (23). If we were to perform our analysis in a three-dimensional elastic periodic setting (e.g. a cubic array of rigid or traction-free spheres), the derivation of (23) would apply mutatis mutandis with i, j ranging from 1 to 3 and the Bloch vector now describing the edges of a tetrahedron.

2.1. Bloch analysis

A key canonical problem that can be solved without recourse to an effective medium approach, and ideal for comparison with the asymptotic theory, is that of elastic waves propagating within an infinite perfectly periodic medium. These waves can be considered on an elementary cell and acquire a phase-shift in, vector, Bloch wavenumber as they pass from one cell to the next, c.f. Fig. 1. One then solves the elastic problem on an elementary cell with Bloch quasi-periodic boundary conditions on the edge of the cell that $\mathbf{u}(1, y) = \exp(2i\kappa_1)\mathbf{u}(-1, y)$ and $\mathbf{u}(x, 1) = \exp(2i\kappa_2)\mathbf{u}(x, -1)$ and similarly for the stresses. These boundary conditions then allow one to work only with a single elementary cell and dispersion relations are found relating frequency Ω to Bloch wavenumber $\boldsymbol{\kappa} = (\kappa_1, \kappa_2)$. For simple geometries, such a cylindrical holes, these have been found using numerical methods or semi-analytical techniques such as multipoles (Zalipaev et al., 2002; Guenneau et al., 2003). From the symmetry of, say, cylindrical holes placed on a square lattice array one can identify the irreducible Brillouin zone (in wavenumber space) c.f. Fig. 1(b) that needs to be considered, ΓMX in our case. Traditionally in solid-state physics dispersion curves are plotted around the exterior paths ΓM, XM and ΓM and these identify key features such as stop-bands, curvature changes

(with consequent group velocity implications) and so on; it is worth mentioning that doing so runs the risk of missing interesting physics (Craster et al., 2012).

Typical Bloch dispersion diagrams are shown in Figs. 3, 5. The asymptotic technique we develop is based about a knowledge of the standing wave solutions that are exactly at the edges of the Brillouin zone: Γ, M and X. In its simplest incarnation the HFH approach generates asymptotic dispersion curves at the edges of the Brillouin zone and these then provide a perfect vehicle upon which to test the theory. Recasting (23) into a perfectly periodic system with Bloch conditions on the elementary cell lead immediately to $f_0(\mathbf{X}) = \exp(i\kappa_j X_j/\epsilon)$ around, say, the wavenumber at point Γ, which leads to the asymptotic representation

$$\Omega \sim \Omega_0 + \frac{T_{ij}}{2\Omega_0}\kappa_i\kappa_j \tag{24}$$

and the coefficients T_{ij} capture the essential physics; essentially identical formulae hold at M and X. The asymptotic technique is more versatile than just generating dispersion curves and it can provide deeper insight into wave phenomena as shown in section 3.2.

2.2. Repeated eigenvalues: Linear asymptotics

Repeated eigenvalues are, as we shall see later, commonplace in specific examples and are particularly relevant to Dirac-like cones (Chan et al., 2012; Antonakakis et al., 2013b) that have practical significance. If we assume repeated eigenvalues of multiplicity p the general solution for the leading order problem becomes,

$$u_{0_i} = f_0^{(l)}(\mathbf{X})U_{0_i}^{(l)}(\boldsymbol{\xi};\Omega_0) \tag{25}$$

where we sum over the repeated superscripts (l) throughout. This alteration of (9) has technical consequences, but the route to an effective description is similar. We multiply the first order equation of (6) by $U_{0_i}^{(m)}$, subtract u_{1_i} multiplied by equation (11) then integrate over the microcell to obtain,

$$f_{0,X_i}^{(l)}A_{iml} + \Omega_1^2 f_0^{(l)}\int_S \rho U_{0_i}^{(l)}U_{0_i}^{(m)}dS = 0. \tag{26}$$

This is now a system of coupled partial differential equations for the $f_0^{(l)}(\mathbf{X})$ on the macroscale and, provided $\Omega_1 \neq 0$, the leading order behaviour of the dispersion curves near the Ω_0 is now linear (these then form Dirac-like cones). These coupled partial differential equations on the long-scale now replace (22) near these frequencies.

For the perfect lattice and Bloch problem, c.f. section 2.1, we set $f_0^{(l)} = \hat{f}_0^{(l)}\exp(i\kappa_j X_j/\epsilon)$ and obtain the following system of equations,

$$\left(i\kappa_j A_{jml} + \Omega_1^2\epsilon B_{ml}\right)\hat{f}_0^{(l)} = 0, \quad \text{for} \quad m = 1, 2, ..., p \tag{27}$$

where,

$$\begin{aligned} A_{jml} = \int_S \mu\left(U_{0_i}^{(m)}(U_{0_i,\xi_j}^{(l)} + U_{0_j,\xi_i}^{(l)}) - U_{0_i}^{(l)}(U_{0_i,\xi_j}^{(m)} + U_{0_j,\xi_i}^{(m)})\right) \\ +\lambda\left(U_{0_i,\xi_i}^{(l)}U_{0_j}^{(m)} - U_{0_i,\xi_i}^{(m)}U_{0_j}^{(l)}\right)dS \end{aligned} \tag{28}$$

and

$$B_{ml} = \int_S \rho U_{0_i}^{(l)}U_{0_i}^{(m)}dS. \tag{29}$$

The system of equations (27) is written simply as,

$$\mathbf{C}\hat{\mathbf{F}}_0 = \mathbf{0}, \tag{30}$$

with $C_{ll} = \Omega_1^2\epsilon B_{ll}$ and $C_{ml} = i\kappa_j A_{jml}$ for $l \neq m$. One must then solve for $\Omega_1^2\epsilon = \pm\sqrt{\alpha_{ij}\kappa_i\kappa_j}$ when the determinant of $\mathbf{C}$ vanishes and the asymptotic relation is,

$$\Omega \sim \Omega_0 \pm \frac{1}{2\Omega_0}\sqrt{\alpha_{ij}\kappa_i\kappa_j}. \tag{31}$$

If Ω_1 is zero, one must go to the next order, and a slightly different analysis ensues, and we treat this next.

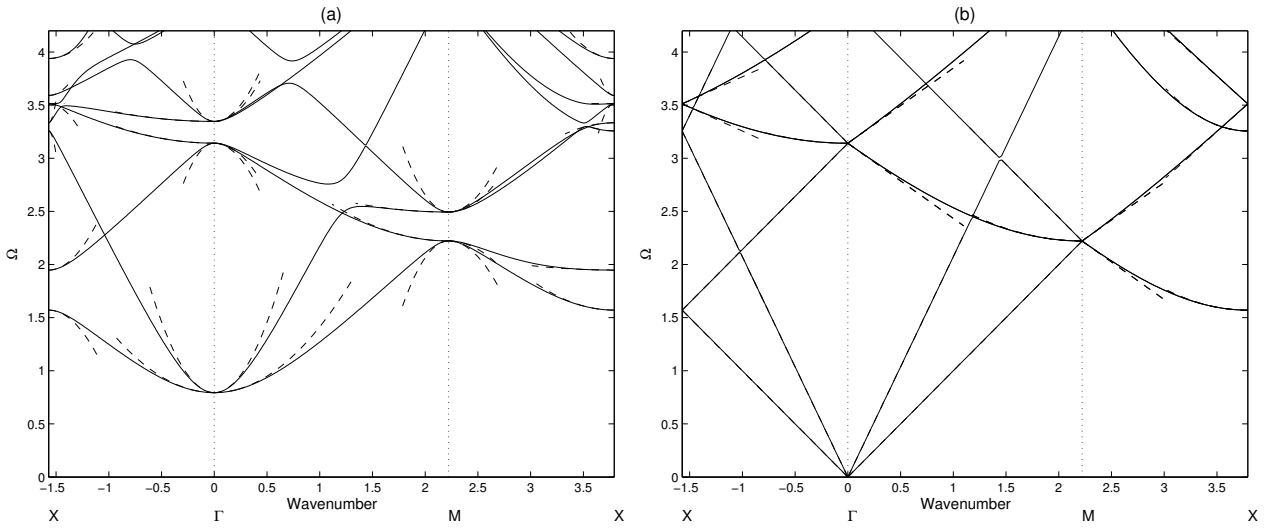

Figure 2: Bloch dispersion curves and HFH asymptotics for cylinders of radius 0.01 in an elementary cell of side 2: (a) Clamped and (b) traction free boundary conditions. The solid lines are from numerical simulations and the dashed lines are from the HFH Eqns. (24, 31) and (36). In some cases, particularly in (b) for the linear asymptotics, the HFH and full numerics are visually indistinguishable.

2.3. Repeated eigenvalues: Quadratic asymptotics

Assuming that Ω_1 is now zero, $u_{1_i} = f^{(l)}_{0,X_j} U^{(l)}_{1_{ij}}$ (we again sum over all repeated (l) superscripts) and advance to second order using (6). Taking the difference between the product of equation (6) with $U^{(m)}_{0_i}$ and $u_{2_i} S_{0_{ij},\xi_j}$, and integrating over the elementary cell, gives a system of coupled partial differential equations,

$$f^{(l)}_{0,X_iX_i} A_{ml} + f^{(l)}_{0,X_kX_j} D_{kjml} + \Omega_2^2 f^{(l)}_0 B_{ml} = 0, \quad \text{for} \quad m = 1, 2, ..., p, \tag{32}$$

where,

$$A_{ml} = \int_S \mu U^{(l)}_{0_i} U^{(m)}_{0_i} dS, \tag{33}$$

$$D_{kjml} = \int_S \Big(\mu \left(U^{(m)}_{0_i} (U^{(l)}_{1_{ik},\xi_j} + U^{(l)}_{1_{jk},\xi_i}) - U^{(l)}_{1_{ik}} (U^{(m)}_{0_{i,\xi_j}} + U^{(m)}_{0_{j,\xi_i}}) + U^{(l)}_{0_j} U^{(m)}_{0_k} \right) \\ + \lambda \left(U^{(l)}_{1_{ik},\xi_i} U^{(m)}_{0_j} - U^{(l)}_{1_{jk}} U^{(m)}_{0_{i,\xi_i}} + U^{(l)}_{0_k} U^{(m)}_{0_j} \right) \Big) dS \tag{34}$$

and

$$B_{ml} = \int_S \rho U^{(l)}_{0_i} U^{(m)}_{0_i} dS. \tag{35}$$

For the Bloch wave setting, c.f. section 2.1, using $f^{(l)}_0(\mathbf{X}) = \hat{f}^{(l)}_0 \exp(i\kappa_j X_j/\epsilon)$ we obtain the following system,

$$\left(-\kappa_i \kappa_i A_{ml} - \kappa_k \kappa_j D_{kjml} + \Omega_2^2 \epsilon^2 B_{ml} \right) \hat{f}^{(l)}_0 = 0, \quad \text{for} \quad m = 1, 2, ..., p \tag{36}$$

and this determines the asymptotic dispersion curves.

2.4. Long wave zero frequency limit

Under traction free boundary conditions on the holes the medium permits wave propagation at frequencies of the order of $\Omega^2 \sim O(\epsilon^2)$; the case of clamped boundary conditions is fundamentally different and the

T_{11}	T_{22}	Ω_0
-0.1826	2.470	2.112
1.6246	-2.4885	3.3317
-196.4900	-0.1476	3.5485
200.6397	-0.6115	3.6216
1.0742	4.9378	4.3847
-28.7271	4.0614	4.5952
27.4797	0.2967	4.6258

Table 1: The first seven standing wave frequencies for a square cell with clamped holes of radius $r = 0.4$ at wavenumber $\boldsymbol{\kappa} = (\pi/2, 0)$ at X, c.f. Fig. 3(a), together with associated values for T_{11} and T_{22}. Opposite signs of T_{11}, T_{22} together with absolute values of similar orders of magnitude yield characteristic type of propagation. If one coefficient is much less in magnitude than the other, e.g. $|T_{11}| \ll |T_{22}|$, then directive propagation emerges in the horizontal and vertical directions. The above coefficients are used in Fig. 6

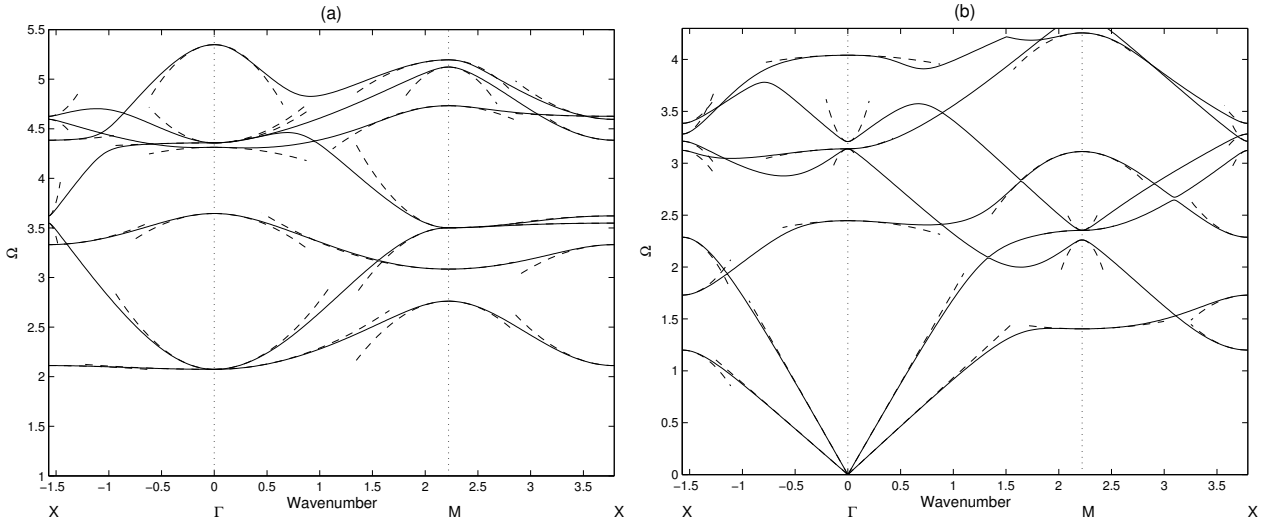

Figure 3: Bloch dispersion curves and HFH asymptotics for cylinders of radius 0.4 in an elementary cell of side 2: (a) Clamped and (b) traction free boundary conditions. The solid lines are from numerical simulations and the dashed lines are from the HFH Eqns. (24, 31) and (36).

material exhibits a zero-frequency stop-band and no long-wave low frequency solution. Note this can have potential applications in shielding elastic waves of very long wavelengths (e.g. seismic waves).

For the traction-free case, the leading order equation is $\sigma_{ij,\xi_j} = 0$ and admits two independent solutions for $u_i = f_0^{(l)}(\mathbf{X})U_{0_i}^{(l)}$, where $U_{0_i}^{(l)}$ are constants. Constant U_0 solutions are inserted in the first order equation to yield $\Omega_1 = 0$. Then we solve for $u_{1_i} = f_{0,X_j}^{(l)} U_{1_{ij}}^{(l)}$ where the first order equation is the same as the leading order but the boundary conditions are $\sigma_{1_{ij}} n_j = 0$. Finally Ω_2 is obtained using equation (36) then inserting $\Omega_0 = \epsilon\Omega_2$ to give the linear asymptotics.

3. Results

We begin by verifying the accuracy of the asymptotic technique by creating asymptotic dispersion curves from (24) and comparing them to full numerical simulations performed using finite elements, before then moving on to investigate some of the broad features and wave phenomena that can arise in elasticity. For definiteness we fix the normalised elastic Lamé parameters λ, μ as $2.3, 1$ respectively, and similarly for the

density $\rho = 1$, in all of the following computations as typical material values. These normalised parameters can be used for elastic media with a Poisson ratio close to 0.35, for instance fused silica, which is drilled to fabricate photonic crystal fibres (in dimensional terms $\rho = 2.2{\times}10^3$ kg m^3, $\lambda = 31.15{\times}10^9$ Pa, $\mu = 16.05{\times}10^9$ Pa).

3.1. Bloch dispersion curves

Typical Bloch dispersion curves, with both the HFH asymptotics (dashed lines) and numerical simulations from finite elements (solid lines) shown are plotted in Figs 2, 3 and 5 for cylindrical inclusions of radii $0.01, 0.4$ and 0.8 respectively. These figures show the clamped inclusions in panels (a) and traction free holes in panels (b); an immediate conclusion is that clamped inclusions have a zero frequency stop-band, in common with Dirichlet inclusions in the acoustic/ polarised electromagnetic analogues, c.f. Antonakakis et al. (2013b), whereas traction-free inclusions share features with the analogous Neumann case at low frequencies, i.e., there is a low-frequency linear response. The zero-frequency stop-band behaviour of the clamped inclusions completely derails the classical homogenisation approach of effective media that requires low frequencies and long waves and the microstructured medium supports no waves in this limit: nonetheless the HFH asymptotics from (24) accurately represent the dispersion curves close to the edges of the Brillouin zone for both clamped and traction-free cases.

For clamped inclusions (Figs 2(a), 3(a) and 5(a)), one recognises that, apart from the zero-frequency stop-band, other stop bands and features from the dispersion curves are striking. Stop-bands correspond to ranges of frequency where waves will not propagate within the medium and so have important physical consequences. The bottom edge of the zero-frequency stop-band moves to higher frequencies as the radii increase and the dispersion curves gradually flatten, this is particularly noticeable for radius 0.8 (Fig. 5(b)). Some of the associated eigenmodes, at Γ, are shown in Fig. 4 with panel (c) showing the eigenmode for the flat band where the two components of U_0 are effectively rotations of each other.

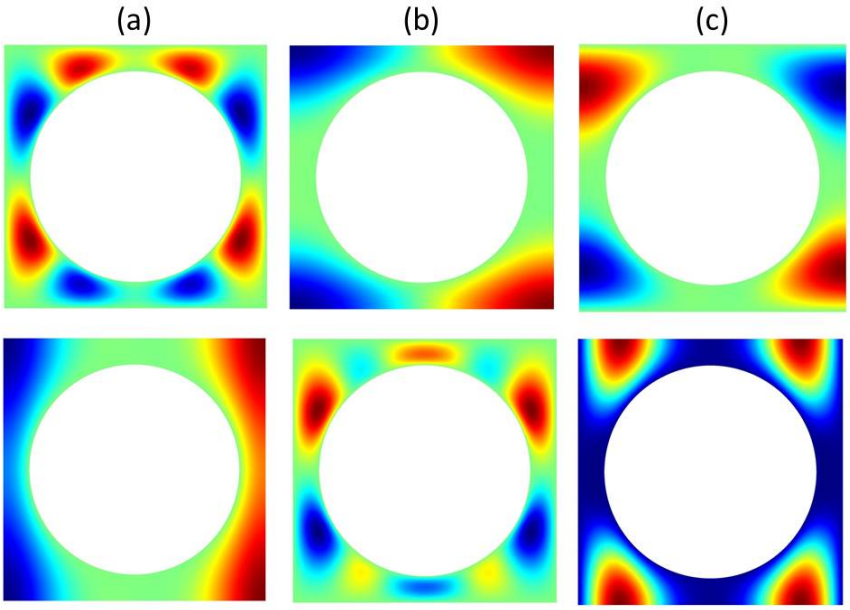

Figure 4: For large cylinders with radius 0.8, the eigenmodes for the first, second and third standing wave frequencies at $\Omega = 4.8053, 5.0762, 5.6985$ and at Γ respectively in (a), (b) and (c), c.f. Table 2 are shown. Column panels separate the different frequencies and rows separate the two components of displacement, namely U_{0_1} and U_{0_2} for the top and bottom rows respectively.

T_{11}	T_{22}	Ω_0
0	2.062	4.8053
−3.6225	0	5.0762
−0.0037	0.0044	5.6985
6.8525	−2.3573	6.2524
0.0120	−4.1465	7.6726
−3.9605	−0.0330	7.8804
5.2294	−23.3779	8.1499
0.0284	−0.0272	8.2729

Table 2: The first eight standing wave frequencies for a square cell with clamped holes of radius $r = 0.8$ at wavenumber $\boldsymbol{\kappa} = (\pi/2, 0)$ at X, c.f. Fig. 5(a), together with associated values for T_{11} and T_{22}. Opposite signs of T_{ii}'s together with absolute values of similar orders of magnitude yield characteristic type of propagation. If one coefficient is almost zero then directive propagation emerges in the horizontal and vertical directions (infinite artificial anisotropy). The above coefficients are used in Figs. 9 and 7

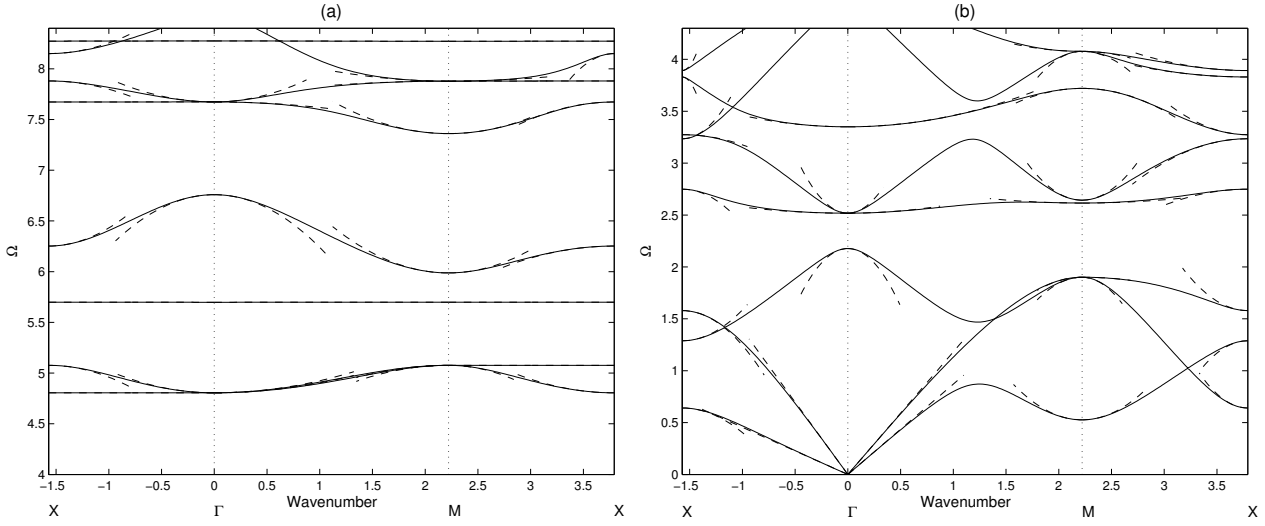

Figure 5: Bloch dispersion curves and HFH asymptotics for cylinders of radius 0.8 in an elementary cell of side 2: (a) Clamped and (b) traction free boundary conditions. The solid lines are from numerical simulations and the dashed lines are from the HFH Eqns. (24, 31) and (36)

Dispersion curves are related to group velocity via the gradient of the curves and changes in curvature and isolated flat, or nearly flat, dispersion curves are useful indicators of interesting and useful phenomena. These features are evident in the figures e.g. the third mode of Fig. 5(a). Flat curves correspond to modes that are "slow" or to directional standing waves. In Fig. 4 we illustrate three of the eigenfunctions at point X of the Brillouin zone for the setting of clamped holes with $r = 0.8$. Notably the first three modes at the standing wave frequencies of $\Omega = 4.8053, 5.0762$ respectively and beginning to be reminiscent of waveguide modes as the flatness of the bands suggests from Fig. 5(a). In Fig. 4(c) the almost completely flat mode has a rotational symmetry for U_{01}, U_{02} and this is an isolated mode for a linear array of cylinders within a waveguide.

For the traction-free cases the numerical dispersion curves have been previously found by Zalipaev et al. (2002); Guenneau et al. (2003) using multipole techniques; at low frequency ($\Omega \sim 0$ near Γ) one obtains two linear dispersion curves that correspond to the effective medium for long waves (see section 2.4). As a general trend, for these traction-free cases of Figs. 2(b), 3(b) and 5(b) one observes that at very small radii, Fig. 2(b), there are no stop-bands and the dispersion curves are almost identical to those for a medium with

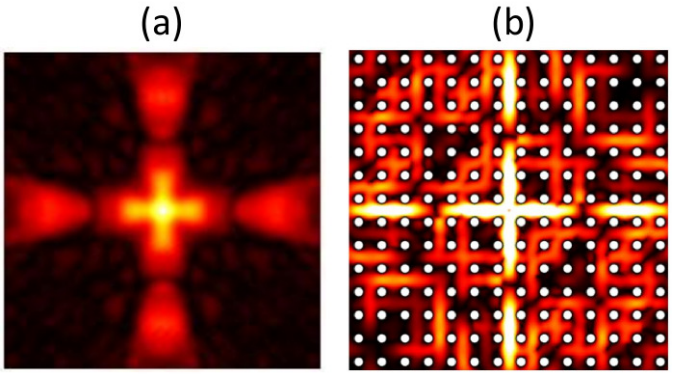

Figure 6: Directive emission in horizontal and vertical directions, caused by a point compressive source at frequency $\Omega = 2.19$, in a doubly periodic array of square cells with circular holes of radius $r = 0.4$, clamped at their surface. c.f Fig. 3(a) first mode at point X. Panel (b) shows FEM calculations and panel (a) reproduces the effects by HFH with $T_{11} = -0.18255$ and $T_{22} = 2.46973$ (see Table 1).

no inclusions; this explains the multiple crossings near, say, $\Omega \sim 2.2$ at wavenumber M. This small radius situation can also be treated using a complementary asymptotic technique, matched asymptotic expansions (Guo and McIver, 2011), valid for very small weakly interacting inclusions. As the inclusion radii increase from 0.4 to 0.8 the multiple crossings become less common and of lower multiciplity, and eventually stop-bands open up. The asymptotic theory works exceptionally well providing accurate curves showing changes in curvature as the hole radius changes, e.g. the lowest mode at M, the emergence of a stop band as hole radius increases and successfully capturing the changes in curvature for, say, the lowest mode at X in Fig. 5(b): indeed all major features of the dispersion diagram are captured.

It is satisfying to note that the asymptotics based upon the scalar f_0 equation capture the detailed behaviour of the dispersion curves and this is strong verification of the approach we have employed. We now move on to using the asymptotics to predict and explain specific phenomena. The power of the asymptotic technique, is that it allows us to replace a microstructured medium by an effective dispersive medium whose elastic properties are encapsulated within the coefficients T_{ij} in the PDE of Eq. (22), or by the coefficients in the coupled cases of repeated roots. The form of the f_0 equation (22) then guides one to anticipate or predict particular features.

3.2. Highly- directional standing waves

Some features of the dispersion diagram, and the asymptotics, reflect the underlying symmetry of the geometry, for instance, if the hole geometry is symmetric then the tensor T_{ij} is purely diagonal. Moreover, at wavenumber position Γ of the Brillouin zone one obtains $T_{11} = T_{22}$ at the isolated standing wave frequencies. However, in general, this is not the case at M or at X where the non-zero elements T_{11} and T_{22} need not be identical nor even have the same sign. For changes in sign, the PDE for f_0 (22) that represents the effective medium changes type from elliptic to hyperbolic with the result that strongly directional waves propagate along the characteristics.

Highly directional waves have been recently identified for simple mass-spring models that originate from solid state physics (Ayzenberg-Stepanenko and Slepyan, 2008; Osharovich et al., 2010; Osharovich and Ayzenberg-Stepanenko, 2012) and at key frequencies one observes directional standing waves that have an interpretation in terms of flat bands in the dispersion curves (Craster et al., 2012). Other discrete systems notably for frames, Colquitt et al. (2012), also exhibit these striking features, and their occurence is shown to be a generic consequence of the underlying HFH asymptotic equations changing from elliptic to hyperbolic (Antonakakis et al., 2013b). Therefore this feature is observed in continuum electromagnetic periodic media too (Craster et al., 2012) and the behaviour predicted using HFH. Here we demonstrate that this highly directional behaviour also occurs in elasticity.

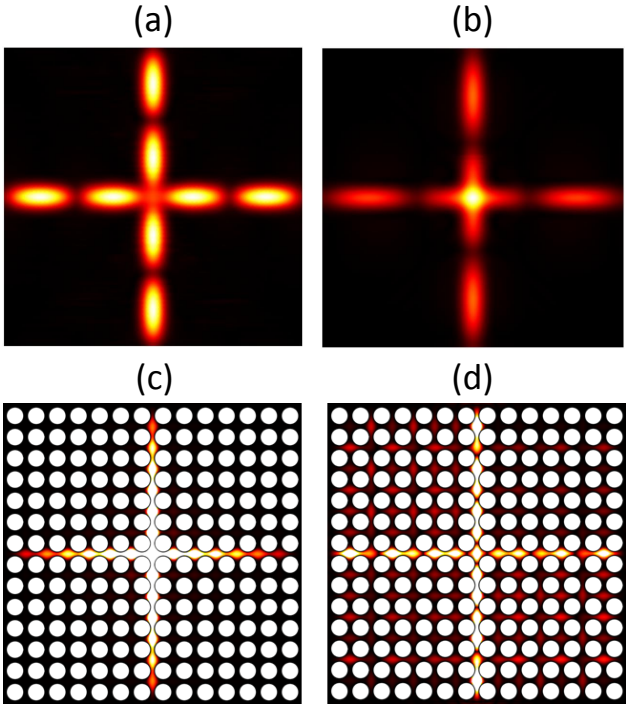

Figure 7: A square array of holes of radius 0.8 is considered. Here we take 196 clamped holes and a compressive source excites the medium at the frequencies of $\Omega = 4.85$ and $\Omega = 5.03$ for panels (a), (c) and (b), (d) respectively c.f. Fig. 5(a). Panels (c) and (d) show FEM simulations and panels (a) and (b) confirm the cross effects with HFH. T_{11}, T_{22} coefficients are given in Table 2 for the first and second modes.

This behaviour is illustrated in Figs. 6, 7 and 9. Starting with radius 0.4 and choosing a frequency ($\Omega = 2.16$) close the first standing wave frequency, 2.11, given in Table 1 we can then use the associated T_{11}, T_{22} to simulate the asymptotic behaviour: here $|T_{11}| \ll |T_{22}|$. It is important to note that due to the symmetry of the circular hole geometry, that we chose to illustrate the theory with, that we only plot, and perform the asymptotics explicitly for standing waves corresponding to the edges of the irreducible Brillouin zone ΓMX. In order to interpret the highly directive fields observed we require the asymptotics at the point N where $\boldsymbol{\kappa} = (0, \pi/2)$, and then the T_{11} and T_{22} coefficients exchange values. The superposition of the two unidirectional effective media then gives the observed bi-directive emission in orthogonal directions. Fig. 6 shows the result from a finite element simulation with a centrally placed compressive source excited at $\Omega = 2.16$ in Fig. 6 (b) together with the corresponding HFH asymptotic simulation in Fig. 6 (a). Clearly both show the same quantitative features of a cross with its arms along the horizontal and vertical directions, as alluded to above this is an immediate consequence of T_{11} and T_{22} having opposite signs and being of different magnitude, in this case being roughly a factor of ten different. This cross-like feature is ubiquitous and arises often, although for the larger radius, $r = 0.8$, that we consider the size of the holes slightly obscures the effect for finite element simulations.

The T_{11}, T_{22} coefficients for $r = 0.8$ at point X of the Brillouin zone are presented for the first two modes of Table 2 where one of the two coefficients is zero. The resulting simulations comparing full numerical simulations and HFH asymptotics are in Figs. 7(a,b,c,d). Clearly such highly anisotropic features are an ubiquitous feature of elastic wave propagation in structured media; they could have important applications in directing and guiding the flow of elastic wave energy through composites.

Figure 8 further illustrates the strong directionality that can be achieved by exciting periodic media at precise frequencies. Here we deliberately chose a case where the $T_{11} = -3.2484$ and $T_{22} = 3.3839$ are of

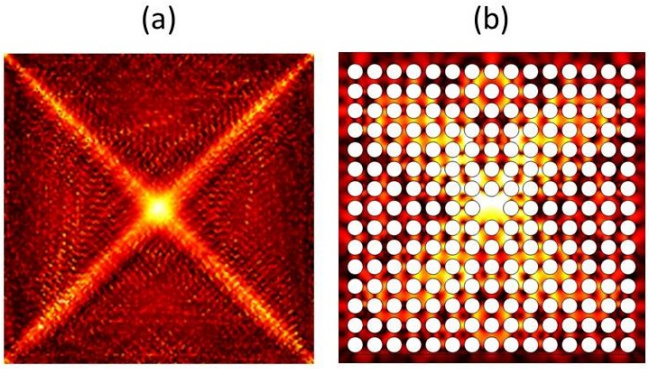

Figure 8: An x-shape is formed by compressive source at frequency $\Omega = 1.51$ for a doubly periodic square array of 225 stress free circular holes with $r = 0.8$ c.f. Fig. 5(b). Panel (b) shows FEM calculations and panel (a) confirms the former with HFH where $T_{11} = -3.2484$ and $T_{22} = 3.3839$. The weakeness of the x-shape in the FEM computations comes from interference with other modes at that frequency c.f. Fig 5(b).

similar magnitude, but opposite sign, to trigger waves in a X shape. The frequency chosen $\Omega = 1.51$ for traction-free holes of radius 0.8 and so also illustrates that this behaviour is not limited to clamped holes.

A natural extension is to consider situations where the magnitude of the coefficients of the tensor are of similar order, but where the signs are still opposite. For instance when the radius is 0.8 and frequency is 6.252, $T_{11} = 6.8525$ and $T_{22} = -2.3572$ c.f. the 4th line of Table 2. In this particular case the characteristics form an angle of 32 degrees with respect to the horizontal and vertical axes as the coefficients do not have an equal absolute value. The resultant weak x-shape effect shown in Fig. 9 comes from the superposition of two effective media, for points $X(\pi/2, 0)$ and $N(0, \pi/2)$ of the Brillouin zone. The HFH simulations shown in Fig. 9(a) and the full numerical simulations shown in Fig. 9(b) share this qualitative feature.

4. Concluding Remarks

HFH theory is here developed for vector wave eqations, specifically for elasticity where the compressive and shear fields and inherently coupled through the boundary conditions. Degenerate cases of multiple roots are treated as well as the classical low frequency homogenisation. Of most importance are the homogenisation results obtained at high frequencies where direct FEM simulations on elastic photonic crystals are in very good qualitative agreement with HFH therefore enabling specific behaviour to be predicted. Both clamped and traction free boundary conditions are treated, but this is not a limitation on the method as using the same formulations for two-phase media, with a continuity condition on displacement and traction between the two phases, can also be treated at the expensive of some algebra . A counter-intuitive, but very important result, is that the ultimate effective medium equation is scalar; this suggests that many complex composite media wave computations can potentially be sidestepped using this formulation.

In addition this approach opens the way for the application of HFH in the full vector Maxwell systems in electromagnetism where a similar approach should yield effective equations. It is notable that many of the phenomena that have recently revolutionised the field of optics can also be shown to occur for elasticity, the strongly directional anisotropy illustrated here being just one example, and a follow-up article illustrating this and using HFH to predict and interpret the behaviour is in preparation.

Acknowledgements

RVC thanks the EPSRC (UK) for their support through research grants EP/I018948/1 & EP/J009636/1 and Mathematics Platform grant EP/I019111/1. SG is thankful for an ERC starting grant (ANAMORPHISM) which facilitates the collaboration with Imperial College London.

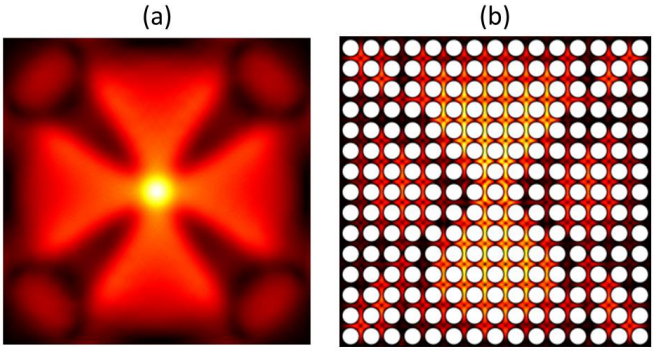

Figure 9: A weak x-shape is formed by compressive source at frequency $\Omega = 6.27$ for a doubly periodic square array of 225 clamped circular holes with $r = 0.8$ c.f. Fig. 5(a). Panel (b) shows FEM calculations and panel (a) confirms the former with HFH where T_{ii} coefficients are found in the fourth row (mode) of Table 2.

References

Allaire, G., Piatnitski, A., 2005. Homogenisation of the Schrödinger equation and effective mass theorems. Commun. Math. Phys. 258, 1–22.

Antonakakis, T., Craster, R. V., 2012. High frequency asymptotics for microstructured thin elastic plates and platonics. Proc. R. Soc. Lond. A 468, 1408–1427.

Antonakakis, T., Craster, R. V., Guenneau, S., 2013a. Asymptotics for metamaterials and photonic crystals. Proc. R. Soc. Lond. A 469, 20120533.

Antonakakis, T., Craster, R. V., Guenneau, S., 2013b. High-frequency homogenisation of zero frequency stop band photonic and phononic crystals. New Journal of Physics 15, 103014.

Ayzenberg-Stepanenko, M. V., Slepyan, L. I., 2008. Resonant-frequency primitive waveforms and star waves in lattices. J. Sound Vib. 313, 812–821.

Bakhvalov, N., Panasenko, G., 1989. Homogenization: Averaging Processes in Periodic Media. Kluwer, Amsterdam.

Bender, C. M., Orszag, S. A., 1978. Advanced mathematical methods for scientists and engineers. McGraw-Hill, New York.

Bensoussan, A., Lions, J., Papanicolaou, G., 1978. Asymptotic analysis for periodic structures. North-Holland, Amsterdam.

Bigoni, D., Guenneau, S., Movchan, A. B., Brun, M., 2013. Elastic metamaterials with inertial locally resonant structures: Application to lensing and localization. Phys. Rev. B 87, 174303.

Birman, M. S., Suslina, T. A., 2006. Homogenization of a multidimensional periodic elliptic operator in a neighborhood of the edge of an internal gap. Journal of Mathematical Sciences 136, 3682–3690.

Brillouin, L., 1953. Wave propagation in periodic structures: electric filters and crystal lattices, 2nd Edition. Dover, New York.

Chan, C. T., Huang, X., Liu, F., Hang, Z. H., 2012. Dirac dispersion and zero-index in two dimensional and three dimensional photonic and phononic systems. Progress In Electromagnetics Research B 44, 163–190.

Colquitt, D. J., Jones, I. S., Movchan, N. V., Movchan, A. B., McPhedran, R. C., 2012. Dynamic anisotropy and localization in elastic lattice systems. Waves Random Complex Media 22, 143–159.

Conca, C., Planchard, J., Vanninathan, M., 1995. Fluids and Periodic structures. Res. Appl. Math., Masson, Paris.

Craster, R. V., Antonakakis, T., Makwana, M., Guenneau, S., 2012. Dangers of using the edges of the Brillouin zone. Phys. Rev. B 86, 115130.

Craster, R. V., Guenneau, S. (Eds.), 2012. Acoustic Metamaterials. Springer-Verlag.

Craster, R. V., Joseph, L. M., Kaplunov, J., 2013. Long-wave asymptotic theories: The connection between functionally graded waveguides and periodic media, to appear Wave Motion http://dx.doi.org/10.1016/j.wavemoti.2013.09.00.

Craster, R. V., Kaplunov, J., Nolde, E., Guenneau, S., 2011. High frequency homogenization for checkerboard structures: Defect modes, ultra-refraction and all-angle-negative refraction. J. Opt. Soc. Amer. A 28, 1032–1041.

Craster, R. V., Kaplunov, J., Pichugin, A. V., 2010a. High frequency homogenization for periodic media. Proc R Soc Lond A 466, 2341–2362.

Craster, R. V., Kaplunov, J., Postnova, J., 2010b. High frequency asymptotics, homogenization and localization for lattices. Q. Jl. Mech. Appl. Math. 63, 497–519.

Gridin, D., Craster, R. V., Adamou, A. T. I., 2005. Trapped modes in curved elastic plates. Proc R Soc Lond A 461, 1181–1197.

Guenneau, S., Craster, R. V., Antonakakis, T., Cherednichenko, K., Cooper, S., 2012. Homogenization techniques for peri-

odic structures. in Gratings: Theory and Numeric Application Editor E. Popov. Institut Fresnel AMU, CNRS, Ch. 11, http://www.fresnel.fr/spip/spip.php?rubrique278.
Guenneau, S., Poulton, C. G., Movchan, A. B., 2003. Oblique propagation of electromagnetic and elastodynamic waves for an array of cylindrical fibres. Proc. Roy. Soc. Lond. A 459, 2215–2263.
Guo, S., McIver, P., 2011. Propagation of elastic waves through a lattice of cylindrical cavities. Proc. R. Soc. Lond. A 467, 2962–2982, doi:10.1098/rspa.2011.0069.
Hoefer, M. A., Weinstein, M. I., 2011. Defect modes and homogenization of periodic Schrödinger operators. SIAM J. Math. Anal. 43, 971–996.
Joannopoulos, J. D., Johnson, S. G., Winn, J. N., Meade, R. D., 2008. Photonic Crystals, Molding the Flow of Light, 2nd Edition. Princeton University Press, Princeton.
John, S., 1987. Strong localization of photons in certain disordered dielectric superlattices. Phys. Rev. Lett. 58, 2486–2489.
Kaplunov, J. D., Rogerson, G. A., Tovstik, P. E., 2005. Localized vibration in elastic structures with slowly varying thickness. Quart. J. Mech. Appl. Math. 58, 645–664.
Kittel, C., 1996. Introduction to solid state physics, 7th Edition. John Wiley & Sons, New York.
Milton, G. W., Nicorovici, N. A., 2006. On the cloaking effects associated with anomalous localised resonance. Proc. Roy. Lond. A 462, 3027.
Nemat-Nasser, S., Willis, J. R., Srivastava, A., Amirkhizi, A. V., 2011. Homogenization of periodic elastic composites and locally resonant sonic materials. Phys. Rev. B 83, 104103.
Nolde, E., Craster, R. V., Kaplunov, J., 2011. High frequency homogenization for structural mechanics. J. Mech. Phys. Solids 59, 651–671.
Norris, A. N., Shuvalov, A. L., Kutsenko, A. A., 2012. Analytical formulation of three-dimensional dynamic homogenization for periodic elastic systems. Proc. R. Soc. Lond. A 468, 1629–1651.
Osharovich, G., Ayzenberg-Stepanenko, M., 2012. On resonant waves in lattices. Functional Differential Equations 19, 163–187.
Osharovich, G., Ayzenberg-Stepanenko, M., Tsareva, O., 2010. Wave propagation in elastic lattices subjected to a local harmonic loading. II. Two dimensional problems. Continuum Mech. Thermodyn. 22, 599–616.
Panasenko, G., 2005. Multi-scale modelling for structures and composites. Springer, Dordrecht.
Parnell, W. J., Abrahams, I. D., 2008. Homogenization for wave propagation in periodic fibre reinforced media with complex microstructure. I - Theory. J. Mech. Phys. Solids 56, 2521–2540.
Pendry, J. B., 2000. Negative refraction makes a perfect lens. Phys. Rev. Lett. 85, 3966–3969.
Russell, P., 2003. Photonic crystal fibers. Science 299, 358–362.
Sanchez-Palencia, E., 1980. Non-homogeneous media and vibration theory. Springer-Verlag, Berlin.
Smith, D. R., Padilla, W. J., Vier, V. C., Nemat-Nasser, S. C., Schultz, S., 2000. Composite medium with simultaneously negative permeability and permittivity. Phys. Rev. Lett. 84, 4184.
Veselago, V. G., 1968. The electrodynamics of substances with simultaneously negative values of ϵ and μ. Sov. Phys. Usp. 10.
Walpole, L. J., 1992. Long elastic waves in a periodic composite. J. Mech. Phys. Solids 40, 1663–1670.
Willis, J. R., 2009. Exact effective relations for dynamics of a laminated body. Mech. Materials 41, 385–393.
Yablonovitch, E., 1987. Inhibited spontaneous emission in solid-state physics and electronics. Phys. Rev. Lett. 58, 2059.
Zalipaev, V. V., Movchan, A. B., Poulton, C. G., McPhedran, R. C., 2002. Elastic waves and homogenization in oblique periodic structures. Proc. R. Soc. Lond. A 458, 1887–1912.
Zolla, F., Renversez, G., Nicolet, A., Kuhlmey, B., Guenneau, S., Felbacq, D., 2005. Foundations of photonic crystal fibres. Imperial College Press, London.